

Numerical modeling of two-dimensional delamination growth in composite laminates with in-plane isotropy

Congzhe Wang, Anastasios P. Vassilopoulos, Thomas Keller^{*}

Composite Construction Laboratory (CCLab), Ecole Polytechnique Fédérale de Lausanne (EPFL), Station 16, Bâtiment BP, CH-1015 Lausanne, Switzerland

ARTICLE INFO

Keywords:

2D delamination
Laminates
Fiber bridging
Cohesive elements
Finite element analysis

ABSTRACT

The two-dimensional (2D) delamination growth in fiber-reinforced polymer (FRP) laminates with in-plane isotropy under Mode I loading condition was numerically investigated using finite element analyses. Two sizes of plate models were developed, focusing on different fracture stages. Cohesive elements were employed to simulate the fracture behavior in the presence of large-scale bridging (LSB). The influences of the pre-crack shape/area, loading zone shape/area and fracture resistance were parametrically studied. It was found that either a flatter pre-crack shape or a flatter loading zone shape could result in higher initial structural stiffness and less uniform distribution of the strain energy release rate (SERR) along the pre-crack perimeter during crack initiation and early propagation. However, they had only a minor effect on the stiffness after full fiber bridging development in all directions. The plates finally achieved constant stiffness, which increased linearly with the fracture resistance. The final crack shape was dependent on the loading zone shape and area, but the effects were relatively weak.

1. Introduction

Delamination is one of the most common damage mechanisms in fiber-reinforced polymer (FRP) materials, which can lead to premature structural failure [1,2]. Among the different fracture modes occurring in delamination, Mode I has received most attention, since it necessitates the least energy for crack initiation and propagation [3,4]. As the delamination in FRP materials grows under Mode I loading, fiber bridging develops as a toughening mechanism, differentiating the fracture behavior from that of other materials [5]. In the presence of fiber bridging, cohesive zone modeling (CZM) is regarded as an appropriate method and has been used extensively in finite element (FE) simulations [6–9], due to its ability to embed process zone mechanics through traction-separation relationships across the crack faces, thus separating the fracture process zone (FPZ) ahead of the crack tip from the fiber bridging zone behind the tip.

The vast majority of works on delamination conducted experimental investigations on standardized beam-like specimens [10–13]. The double cantilever beam (DCB) is the most widely used standardized specimen form for Mode I fracture tests on FRP composites. Nevertheless, problems have been encountered in its application during recent years. As shown in [14], the crack front in DCB specimens is curved instead of being straight and perpendicular to the specimens' longitudinal direction, implying non-uniformity of the distribution of the strain energy release rate (SERR), G , across the width and resulting in an underestimation of the fracture resistance by conventional methods [15,16]. In order to obtain a consistent SERR along the crack front, Jiang et al. [14] modified the DCB specimens using a curved pre-crack front determined by a first order optimization method, which however required more effort.

^{*} Corresponding author.

E-mail address: thomas.keller@epfl.ch (T. Keller).

Nomenclature

1D, 2D	one-dimensional and two-dimensional
A_l	basic loading zone area
A_p	basic pre-crack area
a	radial crack length calculated from plate center to delamination front
a_x, a_y	crack lengths in the major-axis and minor-axis directions of the elliptical pre-crack/loading zone
CFM	continuous filament mat
CLR	crack length ratio
COD	crack opening displacement
CZM	cohesive zone modeling
DCB	double cantilever beam
DIC	digital image correlation system
E_1, E_2, E_3	elastic moduli of FRP laminates
FE	finite element
FEA	finite element analysis
FPZ	fracture process zone
FRP	fiber-reinforced polymer
G	strain energy release rate
G_1, G_2, G_3	shear moduli of FRP laminates
G_{br}	G due to fiber bridging
G_{tip}	G at crack tip
G_{tot}	total G for crack propagation
GFRP	glass fiber-reinforced polymer
K_0	penalty stiffness
LSB	large-scale bridging
LVDT	linear variable differential transducer
SERR	strain energy release rate
γ	rate factor of damage evolution
δ	crack separation
δ_1	virtual crack separation at bridging onset
δ_f	maximum crack separation
$\nu_{12}, \nu_{23}, \nu_{31}$	Poisson's ratios of FRP laminates
σ_c	interfacial strength
σ_{max}	maximum bridging traction

Moreover, the total SERR was found to be thickness-dependent in laminated specimens exhibiting large-scale bridging (LSB) [17,18], i. e. it changed with the stiffness of the DCB specimen arms [12]. Pappas and Botsis [19] eliminated the stiffness dependence implied in the conventional cohesive law by substituting the crack opening displacement (COD) with the product of the COD and the crack opening angle, yet the new relationship proposed is load-type dependent and hence still not a universal method for solving the problem concerned.

Although most of the research was conducted on one-dimensional (1D) beam-like specimens, in reality, the propagation of an embedded crack in most cases is not restricted in one direction but spreads all around its contour, thus producing a 2-dimensional (2D) delamination, with inherent characteristics that cannot be captured by conventional DCB experiments. In a general 2D delamination scenario with a non-circular crack front, the width and curvature of the crack front change continuously with crack propagation. Furthermore, the stiffness of the delaminated region of the laminates gradually increases because of the presence of stretching (in-plane tension stresses due to the boundary conditions of an embedded crack) [20]. As a result, the fracture resistance under 2D crack propagation can be significantly higher than that needed for a 1D crack to propagate in the same material [21,22]. Therefore, it is important to carry out investigations on plate-like specimens that resemble actual fracture scenarios, where cracks propagate in two-dimensions.

Researchers showed particular interest in 2D debond/delamination growth induced by buckling [23–27]. In their analyses however, the critical SERR used was still assumed to be identical to that of the standardized 1D beam-like specimens. If LSB was exhibited, such an assumption may lead to erroneous results. Furthermore, owing to the interaction of local buckling of the laminates above the crack and global buckling of the structural component, the crack tip was under a complex mixed-Mode loading condition, and the fracture behavior for each mode remained unclear. Some research omitted to address this problem and assumed a pure Mode I condition at the crack tip [23,26], which led to a notable deviation between numerical/theoretical results and experimental data. In addition, all the aforementioned research work did not include the effect of fiber bridging. In short, significant differences exist between the research assumptions and actual damage mechanisms in the fracture process of FRP composite structures.

Previously, experimental investigations of the 2D Mode I delamination were conducted on glass fiber-reinforced polymer (GFRP)

laminates with different reinforcements [20]. Subsequently, the specimens reinforced by long continuous filament mats (CFMs) were specifically studied in [22,28] due to their in-plane isotropy and ability to exhibit a considerable amount of fiber bridging. The specimens exhibited the same circular-symmetric load and geometrical configuration, resulting in identical crack propagation in all radial directions. In practice, however, the defect shapes may be random, and the opening forces may not be projected to circular areas. Therefore, the crack propagation may lose the symmetry and instead present a more complex pattern. On the other hand, the numerical model employed in [22] has some limitations in terms of the simplification of the constraints. To the best of the authors' knowledge, no other work has discussed the effect of fiber bridging within the framework of 2D delamination.

The objective of this work was the establishment of an improved numerical approach for 2D delamination analysis and the parametric investigation of the 2D delamination behavior of FRP laminates with different pre-crack and loading zone shapes. For this purpose, the experimental data concerning CFM specimens from [20] were used for the model development. Two sizes of plate models were developed using the commercial finite element analysis (FEA) software ABAQUS 6.14-1 under academic license, each composed of several sub-groups with different pre-crack/loading zone configurations and various fracture resistances. Cohesive elements were employed to simulate the fracture behavior considering the effect of fiber bridging.

2. Previous experiments

Similarly to [22], the two CFM specimens described in [20] were selected for the numerical model development in this work, i.e. the experimental load-opening displacement and crack length-opening displacement curves were used for the calibration of the cohesive law. The experimental set-up and results are therefore summarized in the following for clarification purposes.

The two specimens, referred to as CFM1 and CFM2, contained six layers of CFM reinforcement with a laminate thickness of 7.50 mm and 6.99 mm respectively. As shown in Fig. 1b, a 13- μ m-thick Teflon film with a diameter of 180 mm was placed at the center to create an embedded pre-crack, and a pair of 1.2-mm-thick steel inserts with a diameter of 100 mm, located on the upper and lower sides of the Teflon film, were used to distribute the opening load transferred by a set of steel bolts at the loading line (with a diameter of 70 mm) and a pair of external steel blocks. The experiments were performed under displacement control at a rate of 1.5 mm/min using a W + B electromechanical machine of 50-kN capacity. The load and opening displacement were obtained directly from the machine. The crack front was monitored, thanks to the transparency of the material, in different directions by three measuring systems, i.e. a 3D Digital Image Correlation System (DIC), a digital camera and visual measurements. In addition, four Linear Variable Differential Transducers (LVDTs) were placed at the plate corners to monitor the corresponding displacements. Full details of the material properties, specimen configuration, infusion process and experimental set-up can be found in [20].

The experimental load-opening displacement curves of CFM1 and CFM2 are presented in Fig. 2, along with the points denoting the crack lengths, i.e. the radial distance from the plate center to the crack front. At each recorded displacement level, a total of seven points were obtained in seven directions, see Fig. 3. Increasing loads, even after crack initiation, were observed as a result of a continuously increasing crack front width and a consequently disproportionate increase in the propagation area. The crack remained in the mid-plane and propagated in a circular symmetric manner as expected for an in-plane isotropic reinforcement, as shown Fig. 3.

3. Numerical models and parameters

Based on the CFM specimens described above, three models were developed successively: the first one, a detailed finite square plate

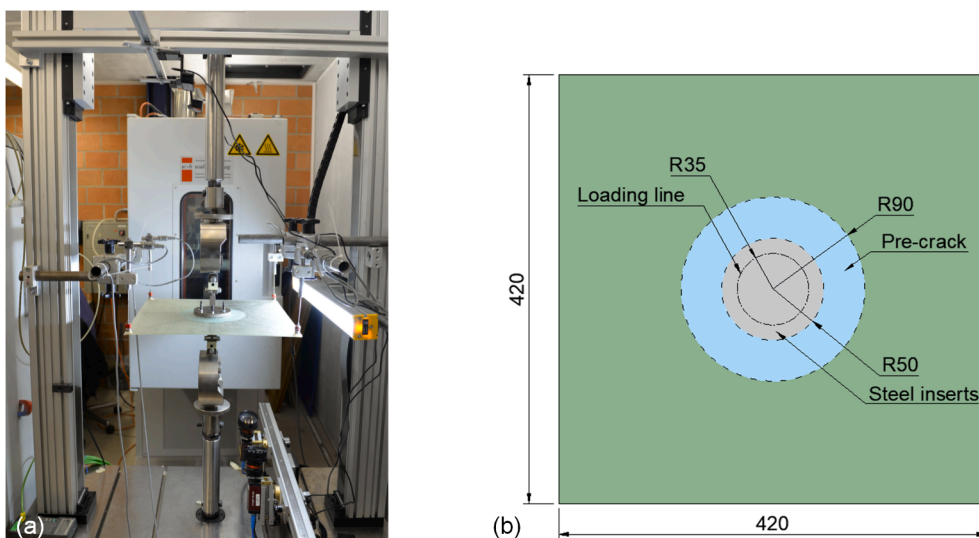


Fig. 1. Experimental set-up: (a) overview; (b) specimen configuration (units in mm) [20].

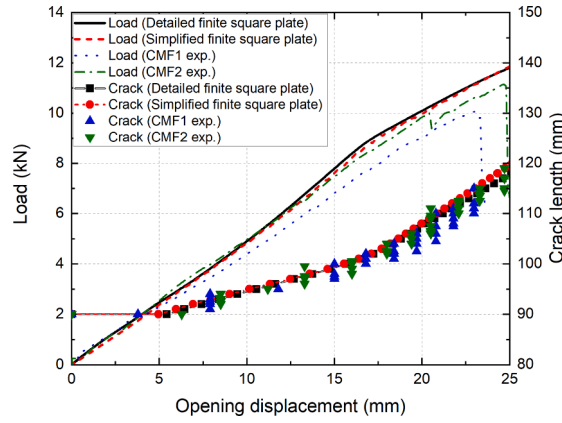


Fig. 2. Experimental and numerical load and crack length vs opening displacement curves.

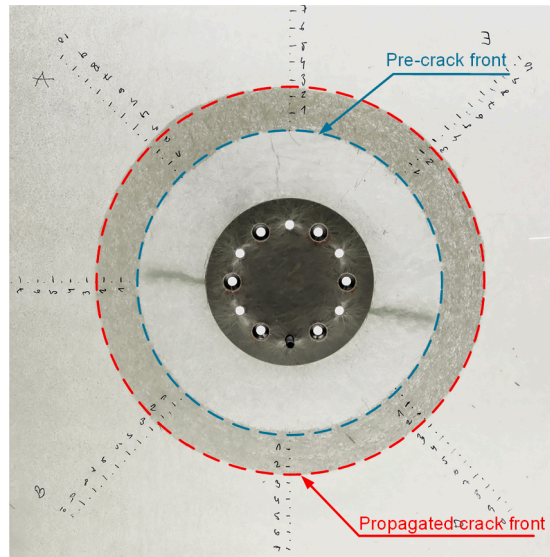


Fig. 3. Typical crack propagation pattern (CFM2).

model, intended for the simulation of the experiments and determination of the cohesive law; the second one, a simplified finite square plate model, intended for the investigation of the 2D fracture behavior at the initiation and early propagation stages; and the third one, a simplified semi-infinite circular plate model, intended for the investigation of the 2D fracture behavior after a certain degree of propagation.

3.1. Detailed finite square plate model and cohesive law

The detailed finite square plate model is shown in Fig. 4a, which had the same dimensions as specimen CFM1 ($420 \times 420 \times 7.5$ mm). In this model, the loading system, i.e. the inserts and bolts, were simulated explicitly. Geometrical nonlinearity was considered to take into account large deformation effects, and the plasticity of the steel inserts was included due to the large plastic deformation observed in the experiments. Considering the symmetry, only one quarter of the plate cut by the diagonal planes was modeled, with symmetric boundary conditions applied accordingly. The external boundary conditions were applied to the bolts, i.e. all degrees of freedom were constrained, as in the experiments. The bolts were modeled as rigid bodies for simplicity, and the contact between the bolts, inserts and laminates was simulated as “hard contact”. The laminate was discretized at the cracking plane, i.e. the mid-plane, into two halves, each meshed with three layers of eight-node continuum shell elements with reduced integration (CS8R) for most regions except for the central part, where the insert replaced the innermost layer. Six-node continuum shell elements with reduced integration (CS6R) were used for the inserts and the central part of the laminates in contact with them in order to achieve comparable element size in this fan-shaped region. A single zero-thickness layer of eight-node 3D cohesive elements (COH3D8) was placed at the mid-plane to connect the uncracked region of the plate and simulate the fracture behavior, with a radial dimension of 1 mm in the

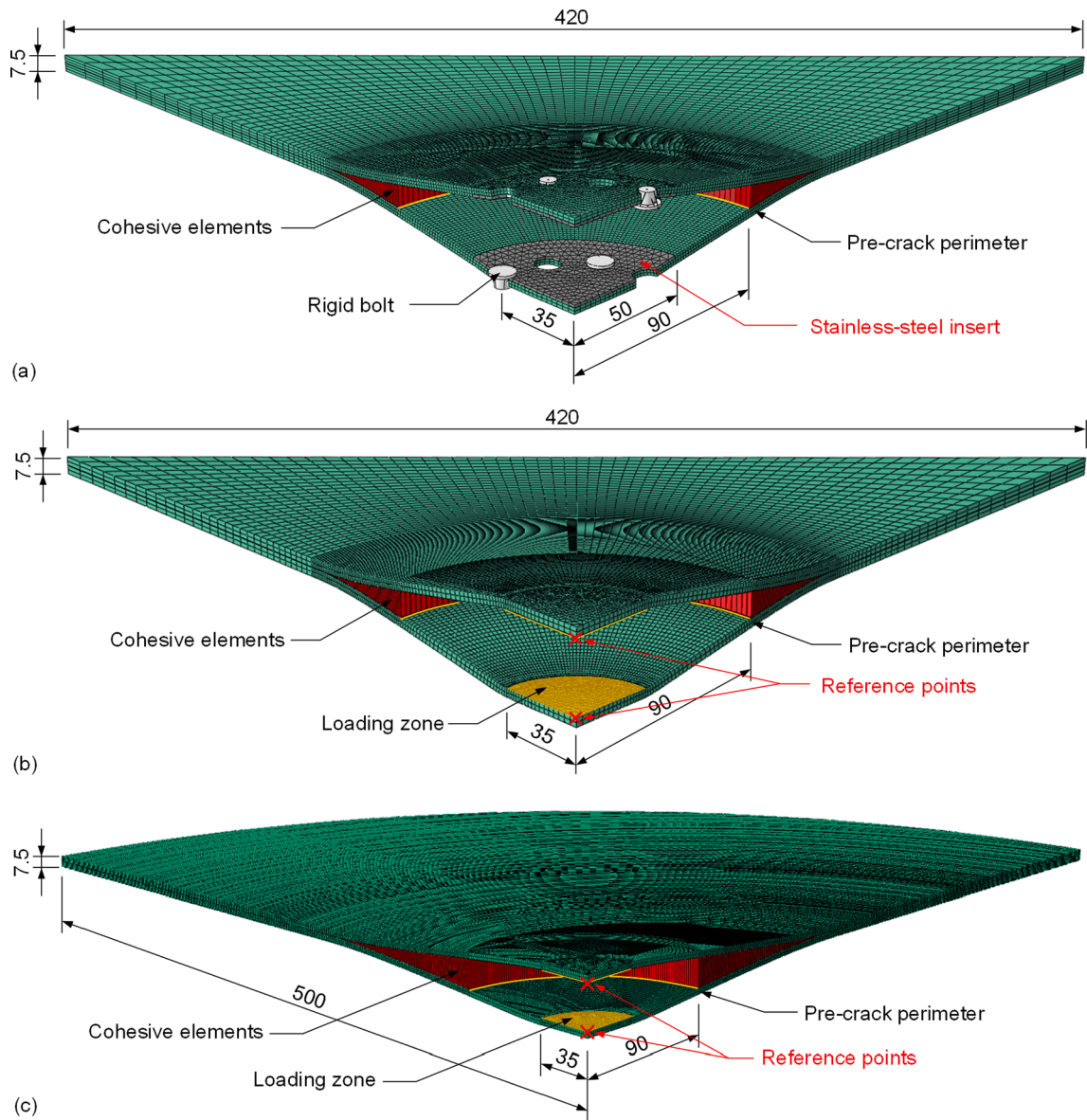


Fig. 4. FE models after some deformation with undeformed dimensions: (a) detailed finite square plate model; (b) simplified finite square plate model; (c) simplified semi-infinite circular plate model (units in mm).

crack-propagation region and a larger size beyond, which guaranteed a minimum of 10 elements in the cohesive zone length throughout the analysis in order to capture the correct distribution of tractions [29]. In total, the model comprised 55,766 nodes and 48,120 elements. Table 1 lists the elastic properties of the laminates, which were derived analytically and then calibrated with experimental data from DCB tests (see [22]). The inserts (stainless steel 304L) were simulated using the Ramberg–Osgood model [30] with material properties taken from [31]. A vertical displacement of up to 25 mm (the approximate experimental ultimate displacement) was applied to the upper bolts to perform the loading process.

A cohesive law that is able to consider LSB, as described in Fig. 5 [22,32], was employed by means of a user material subroutine (VUMAT) written in FORTRAN programming language [33]. The softening part can be divided into two segments: (1) the linear

Table 1
Engineering constants of laminated plates.

$E_1 = E_2$	E_3	G_{12}	$G_{23} = G_{31}$	ν_{12}	$\nu_{23} = \nu_{31}$
8.64 GPa	4.68 GPa	3.25 GPa	1.54 GPa	0.33	0.30

softening segment, which corresponds to the small FPZ ahead of the crack tip, and (2) the exponential softening segment, which corresponds to the fiber bridging zone. Accordingly, the total SERR for crack propagation, G_{tot} , can be split into G_{tip} , the SERR at the crack tip (i.e. the SERR required for crack initiation), and G_{br} , the SERR due to fiber bridging, respectively. Among the cohesive parameters, K_0 (the penalty stiffness), σ_c (the interfacial strength), σ_{max} (the maximum bridging traction) and G_{tip} were taken directly from [22], since the former two serve mainly computational purposes, i.e. saving computational effort and reducing potential error, and the latter two are material properties [6,18,29]. The virtual separation at bridging onset, δ_1 , was subsequently derived by using the area relationship between G_{tip} and the other parameters. Thus, two remaining parameters required to define the cohesive law, δ_f (the maximum separation) and γ (rate factor of damage evolution), were estimated by iterative FEA to achieve a best fit of the numerical load-opening displacement and crack length results with the experimental data. The full set of parameters obtained is summarized as follows: $G_{\text{tot}} = 2.8 \text{ kJ/m}^2$, $G_{\text{tip}} = 0.4 \text{ kJ/m}^2$, $G_{\text{br}} = 2.4 \text{ kJ/m}^2$, $K_0 = 100,000 \text{ MPa/mm}$, $\sigma_c = 25.2 \text{ MPa}$, $\sigma_{\text{max}} = 5 \text{ MPa}$, $\delta_1 = 0.027 \text{ mm}$, $\delta_f = 1.58 \text{ mm}$ and $\gamma = 0.137$. The numerical load-opening displacement and stiffness-opening displacement curves showed overall good agreement with the experimental results in terms of the load levels, crack length evolutions, the turning points on the curves at an opening displacement of around 17.5 mm, and the slopes of the load-opening displacement curves after the turning points, as shown in Fig. 2. The slight deviation in the second half of the curves was due to the absence of intralaminar damage simulation. Indeed, local damage was observed in the experiments in laminates around the bolt holes and inside the pre-crack region (see Fig. 3). It is possible to include such damage through improvement of the constitutive relationship and adding extra damage criteria in the bulk material to be obtained from a new set of material tests. However, considering that the main objective of this work was the numerical investigation of the 2D fracture behavior rather than the accurate simulation of a specific experiment, intralaminar damage was omitted in the FEA.

3.2. Simplified finite square plate model and parameters

After determination of the CZM parameters, the detailed finite square model was simplified in terms of the loading system in order to alter the pre-crack and loading zone shapes for the following parametric investigations. The new model, hereafter referred to as “simplified finite square plate model”, is presented in Fig. 4b. In this model, the loading system was not established explicitly, but instead simulated by applying semi-rigid constraints to the pre-crack surfaces inside the bolting line, i.e. the loading zone. Specifically, the vertical displacement and all rotational displacements of the nodes on the surfaces were coupled with two reference points, while in-plane deformation was allowed. Boundary conditions were applied directly to the reference points, constraining all degrees of freedom with a 25-mm vertical displacement on the upper point. Two layers of CS8R elements were generated for each of the half-plates (CS6R elements were used inside the range of the loading zone instead), which proved to be sufficient after a sensitivity analysis. The other simulation techniques were taken from the detailed finite square plate model. The simplified model comprised 43,997 nodes and 35,780 elements. The load-opening displacement and crack length-opening displacement curves, shown in Fig. 2, were compared with those of the detailed model and experiments. The results from the simplified model were similar to those of the detailed model and also agreed well with the experimental results.

Up to this point, the models were used to reproduce the experiments, from which circular symmetry was always observed due to the symmetric set-up and the in-plane isotropy of the material. This is however not representative of a general delamination scenario, where the defect might be of random shape and the opening forces do not necessarily act on a circular loading zone. Therefore, based on the simplified finite square plate model, four more plates of the same dimensions as specimen CFM1 were modeled with altered pre-crack shape or loading zone shape to investigate the effect of these two parameters on the 2D delamination growth. The total of five simplified finite square plates were sorted into two groups, as shown in Fig. 6. In the first group, the specimens' pre-crack shapes vary from a circle to ellipses of different aspect ratios while maintaining equal circumference, which is regarded as an analogy of the pre-crack width in beam-like specimens. In the second group, different loading zone shapes were selected with the same area in order to

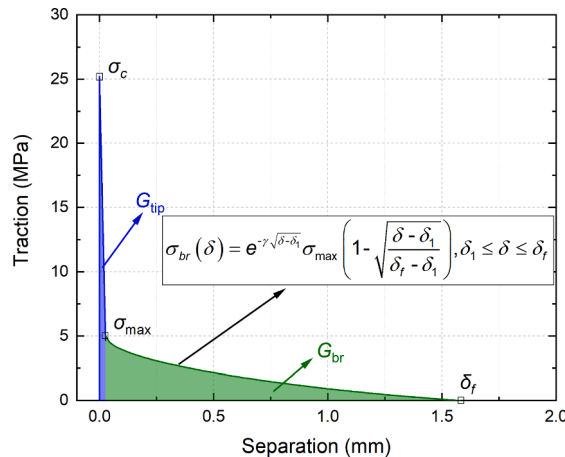


Fig. 5. Traction-separation law (according to [22]).

achieve an equivalent loading condition in terms of the distributed opening loads, and the same circular pre-crack was maintained.

In Fig. 6, the first component of the labels indicates the pre-crack shape of the specimen, e.g. “C90” denotes a circular pre-crack with a radius of 90 mm, while “E2/1” denotes an elliptical pre-crack with an aspect ratio of 2:1; the second component indicates the loading zone shape; and the last component, “S”, denotes “simplified finite square plates”.

3.3. Simplified semi-infinite circular plate model and parameters

In some of the simplified finite square plates fiber bridging was not fully developed in all directions at the end of the loading process. Indeed, the delamination growth was limited by the plate size and shape, as was also the case in the experiments described in [20]. To be specific, if the loading proceeded further, the plate edges would start to have an impact, i.e. the crack would propagate too close to the edges, and the outer intact part of the plate would no longer be able to sustain the circumferential compression forces induced by stretching, leading to unstable crack propagation. On the other hand, if the plate sizes were enlarged without other modifications, stability problems would soon occur due to the circumferential compression in the laminates. Therefore, a new circular plate model was developed from the simplified finite square plate model with an enlarged size, reaching a diameter of 1000 mm while maintaining the same nominal thickness (7.5 mm), as shown in Fig. 4c. Based on this model, hereafter referred to as “simplified semi-infinite circular plate model”, different combinations of pre-crack shape/area, loading zone shape/area and G_{tot} were considered in order to investigate the influences of defect geometry, loading patterns and fiber bridging extent respectively. In addition, the elastic moduli employed were increased to ten times those of the previous models in order to delay the occurrence of instability. The enlarged moduli were chosen so that they are sufficiently high to provide a notable delay in buckling but not too high in case the delamination growth behavior changes (since G_{tot} is still within its original magnitude), which will be examined below. Approximately 323,000 nodes and 282,000 elements were generated for each model, and an opening displacement of up to 100 mm was applied.

In order to comprehensively investigate the effects of the different parameters, several groups of simplified semi-infinite circular plates were established, as shown in Fig. 7. In the first group, the plates have different pre-crack shapes of equal circumference (the first row in Fig. 7). In the second group, the pre-crack shapes also vary, but maintaining the same area, A_p , instead of circumference (the second row in Fig. 7), considering that the crack area is one of the basic physical variables in fracture mechanics. In the third group, the plates again have different pre-crack shapes of the same area, but this time the area is twice the previous value, i.e. $2A_p$ (the third row in Fig. 7). In the fourth group, different loading zone shapes with the same area, A_l , were selected while maintaining the same circular pre-crack (the fourth row in Fig. 7). And in the fifth group, the plates also have different loading zone shapes of the same area, but this time the area is twice the previous value, i.e. $2A_l$ (the fifth row in Fig. 7). Additional groups were developed by changing the fracture resistance of the group of different loading zone shapes with the same basic area from the basic value ($G_{tot} = 2.8 \text{ kJ/m}^2$) to other levels (i.e. 1.4 kJ/m^2 and 4.2 kJ/m^2 , which are 0.5 and 1.5 times the basic value respectively). Extra levels of fracture resistance (i.e. 0.42 kJ/

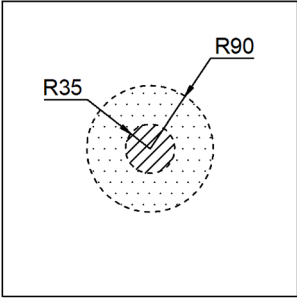
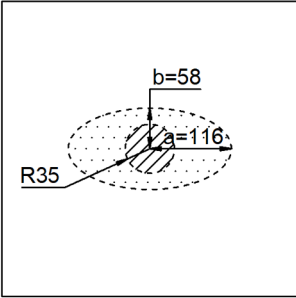
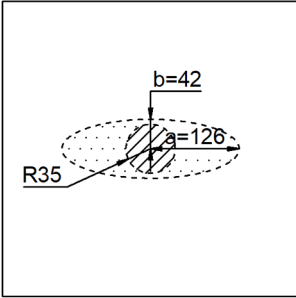
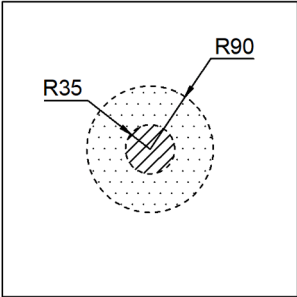
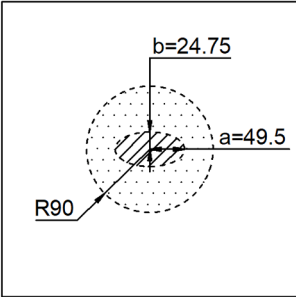
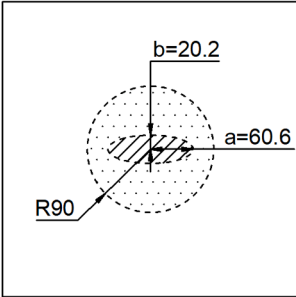
Group	Reference model	Model variations	
Different pre-crack shapes (same circumference)			
	C90-C35-S	E2/1-C35-S	E3/1-C35-S
Different loading zone shapes (same area)			
	C90-C35-S	C90-E2/1-S	C90-E3/1-S

Fig. 6. Model list of simplified finite square plates (dashed area indicates loading zone, and dotted area indicates pre-crack).

Group	Reference model	Model variations		
Different pre-crack shapes (same circumference)				
Different pre-crack shapes (same basic area, A_p)				
Different pre-crack shapes (same doubled area, $2A_p$)				
Different loading zone shapes (same basic area, A_l)				
Different loading zone shapes (same doubled area, $2A_l$)				

Fig. 7. Model list of simplified semi-infinite circular plates (dashed area indicates loading zone, and dotted area indicates pre-crack).

m^2 , 0.7 kJ/m^2 and 5.6 kJ/m^2 , which are 0.14, 0.25 and 2.0 times the basic value respectively) were also assigned to the plate that has a circular pre-crack and an elliptical loading zone with an aspect ratio of 3:1. Variations of G_{tot} were achieved by modifying the two bridging parameters, δ_f and γ in Fig. 5, and thus the initiation part of the cohesive law remained unchanged.

Regarding nomenclature, the first two components of the label follow the same rule as for the simplified finite square plates, i.e. they indicate the pre-crack shape and loading zone shape, respectively. A prime symbol, “'”, was placed after “E (elliptical)” in the first component for the groups that have different pre-crack shapes of the same area (the second and third groups) in order to differentiate them from the plates with different pre-crack shapes of the same circumference (the first group). The additional “2” before “C (circular)” or “E (elliptical)” in the first component indicates the doubled pre-crack area for the corresponding plates (the third group). And likewise, the additional “2” before “C” or “E” in the second component indicates the doubled loading zone area. The third component denotes the fracture resistance, i.e. “1.0G” refers to the basic value of 2.8 kJ/m^2 , and correspondingly, “0.14G”, “0.25G”, “0.5G”, “1.5G” and “2.0G” refer to 0.42 kJ/m^2 , 0.7 kJ/m^2 , 1.4 kJ/m^2 , 4.2 kJ/m^2 and 5.6 kJ/m^2 respectively. In total, 23 simplified

semi-infinite circular plate models were derived.

4. Numerical results and discussion

4.1. Effect of pre-crack shape

To better describe the 2D delamination growth in the plates with elliptical pre-crack or loading zone, two orthogonal directions were selected for investigation, i.e. the major-axis direction and the minor-axis direction. Accordingly, the crack lengths in these directions, calculated radially from the plate center to the delamination front, are denoted as a_x and a_y respectively, as shown in Fig. 8.

The load-opening displacement and crack length-opening displacement curves for different pre-crack shapes at the initiation and early propagation stages are presented in Fig. 9 (results from simplified finite square plate models C90-C35-S, E2/1-C35-S and E3/1-C35-S). The evolution of a_x and a_y can be regarded as the upper and lower bounds of the entire crack propagation, i.e. the curves for other directions will always lie in between (i.e. the solid area in Fig. 9). In addition, the points indicating the crack initiation (i.e. G reaches G_{tip}) and full fiber bridging (i.e. G reaches G_{tot}) for the orthogonal directions are also shown on the corresponding crack length-opening displacement curves. Correspondingly, four specific fracture states can be identified in terms of 2D delamination growth as follows:

- (1) Crack initiation in one direction, i.e. G of the first point on the pre-crack perimeter reached G_{tip} ;
- (2) Crack initiation in all directions, i.e. G of the last point on the pre-crack perimeter reached G_{tip} ;
- (3) Full fiber bridging in one direction, i.e. G of the first point on the pre-crack perimeter reached G_{tot} ;
- (4) Full fiber bridging in all directions, i.e. G of the last point on the pre-crack perimeter reached G_{tot} .

For plates with elliptical pre-crack/loading zone, “the first point” refers to that in the direction with the shortest distance between the pre-crack front and the loading zone edge, i.e. y direction in Fig. 8a and x direction in Fig. 8b, and “the last point” refers to that in the direction with the longest distance between the pre-crack front and the loading zone edge, i.e. x direction in Fig. 8a and y direction in Fig. 8b. Note that the sequence of the states was determined by the model’s geometry configuration. For instance, for model C90-C35-S, states (1) and (2) overlapped due to circular symmetry, as did states (3) and (4); for model E2/1-C35-S and E3/1-C35-S, state (3) occurred prior to state (2) (see the displacement levels of the marked points in Fig. 9), and state (4) was not yet reached at the end of the loading process due to the limited propagation.

It can be observed from Fig. 9 that as the pre-crack shape varied from a circle to a flat ellipse, the initial stiffness distinctly increased. This difference was attributed to the geometrical configurations of the plates. Specifically, the shortest distance between the pre-crack front and the loading zone edge decreased rapidly from 55 mm for model C90-C35-S to around 7 mm for model E3/1-C35-S, which made the major contribution to the overall stiffness of the whole structure at the beginning of the loading. As the loading continued, the three load-opening displacement curves began to converge. At the end of the loading process, they became almost parallel with equal stiffness, showing that the differences in structural response caused by different pre-crack shapes were disappearing. A similar conclusion can be drawn from the crack length-opening displacement curves. The a_x and a_y curves were converging after the crack initiated in all directions, indicating that the delamination shape was changing towards a circle, i.e. the shape of the loading zone, and the effect of the pre-crack shape was waning. By subtracting the crack length at crack initiation (i.e. the pre-crack length) from that at full fiber bridging, the initial bridging lengths in the orthogonal directions can be obtained respectively. It was found that the initial bridging lengths differed in different configurations of this group.

The load-opening displacement and stiffness-opening displacement curves for the different pre-crack shapes now including crack propagation were plotted in Fig. 10 (results from simplified semi-infinite circular plate models C90-C35-1.0G, E2/1-C35-1.0G and E3/1-C35-1.0G, with the latter curves being the first derivate of the former ones). The load curves were plotted up to an opening displacement of 60 mm, after which instability occurred generally. In the simulations, the stability status was tracked by the vertical displacement of the plate edges. The stiffness curves, which are more sensitive to the stability of the plates, were only plotted up to a vertical line that marks the opening displacement level where the edge of the first plate in the group failed to remain horizontal (at 54 mm in this case).

The shapes of the curves at the initiation and early propagation stages are similar in Figs. 9 and 10 (although the load levels in the

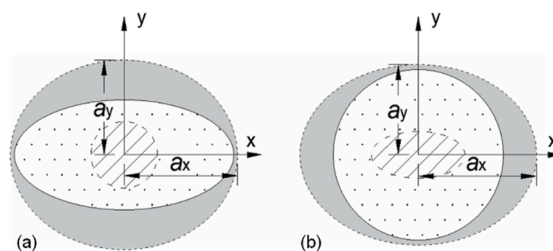


Fig. 8. Description of directions for crack length calculation: (a) plates with elliptical pre-crack and circular loading zone; (b) plates with circular pre-crack and elliptical loading zone.

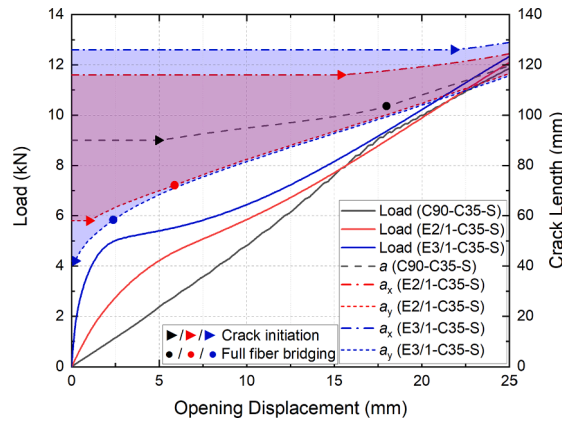


Fig. 9. Load and crack length vs opening displacement curves during crack initiation and early propagation for different pre-crack shapes (simplified finite square plate results).

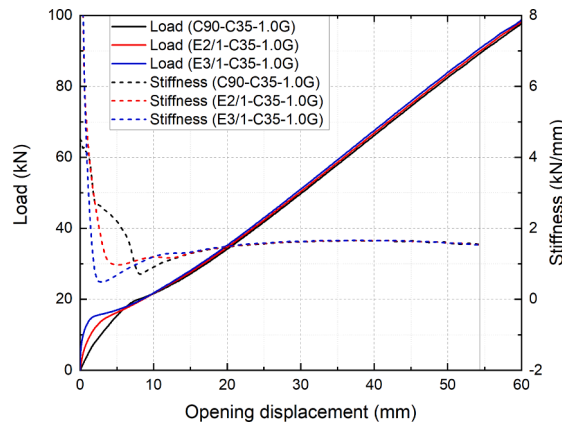


Fig. 10. Load and stiffness vs opening displacement curves during crack initiation and propagation for different pre-crack shapes (simplified semi-infinite circular plate results).

latter case are several times higher), indicating similar fracture behaviors. It is thus logical to assume that the fracture behavior of the simplified semi-infinite circular plates, after a certain extent of propagation, will also be similar, i.e. representative, despite the artificially enlarged moduli. As the models allowed larger displacements before any instability problems arose, it was feasible to achieve full fiber bridging in all directions.

The structural response can be better understood from the stiffness-opening displacement curves. All three plates went through an initial rapid softening stage, followed by a general mildly stiffening stage, and finally reached a state where stiffness remained constant. Three main different mechanisms affecting the specimens' stiffness could be distinguished, i.e. stretching, fiber bridging and crack propagation, with the first two being stiffening mechanisms and the third being a softening mechanism. The softening mechanism prevailed down to the minimum points of the stiffness curves, and then on the upward part of the curves the stiffening mechanisms became dominant until the constant-stiffness state was reached. The final constant stiffness indicates the balance between the stiffening and softening mechanisms. For the circular pre-crack shape (model C90-C35-1.0G), the minimum point (at opening displacement of 7.7 mm) corresponded to the onset of full fiber bridging in all directions. For the models with elliptical pre-crack, on the other hand, the minimum points correspond to none of the aforementioned fracture states. After full fiber bridging was reached in all directions, all three stiffness curves matched, which shows that the pre-crack shape has only a minor effect on the final constant stiffness of the system.

The G values along the pre-crack perimeter at the above-defined four specified fracture states (i.e. (1) crack initiation in one direction (red), (2) crack initiation in all directions (blue), (3) full fiber bridging in one direction (green), and (4) full fiber bridging in all directions (orange)) were normalized over G_{tot} (i.e. 2.8 kJ/m^2) and plotted in a polar coordinate system for both simplified finite square plates and simplified semi-infinite circular plates with elliptical pre-crack, as shown in Fig. 11. Results from models E2/1-C35-S (solid lines) and E2/1-C35-1.0G (dashed lines) were summarized together in Fig. 11a, since they both have the same pre-crack and loading zone configuration, and likewise models E3/1-C35-S and E3/1-C35-1.0G in Fig. 11b. The corresponding opening displacement levels at which the states were reached are also presented in the legends. Thus, the G -level on the pre-crack perimeter in any direction can be radially read from the curve for the fracture states concerned (e.g. a value of 1.0 signifies that full fiber bridging had developed

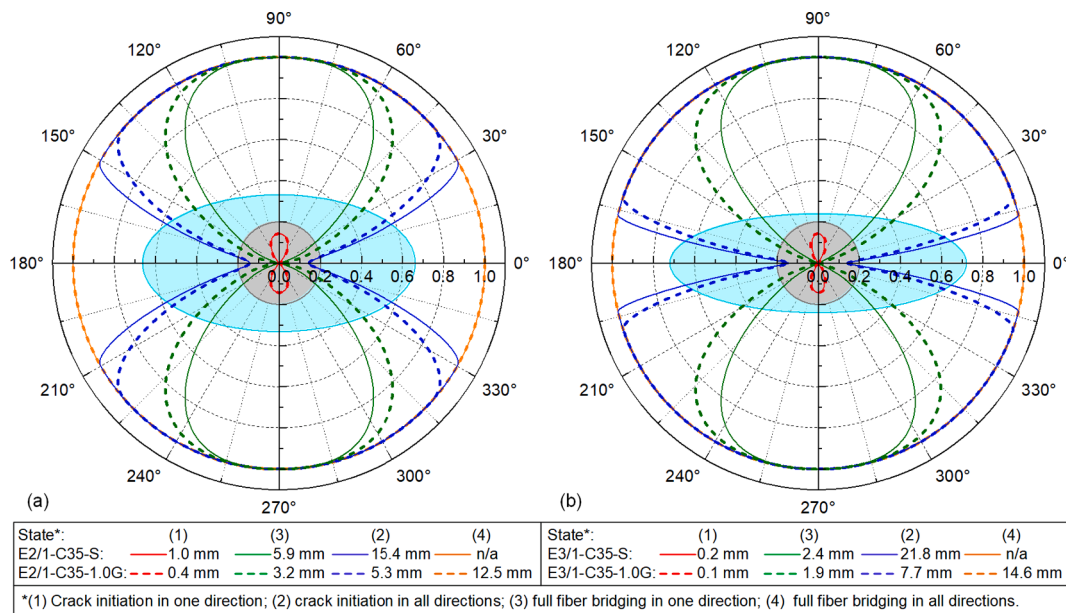


Fig. 11. Normalized G -distribution curves along pre-crack perimeter in plates with elliptical pre-crack at different fracture states: (a) E2/1-C35-S and E2/1-C35-1.0G; (b) E3/1-C35-S and E3/1-C35-1.0G.

in this direction). In addition, the propagated crack shapes in model E3/1-C35-1.0G at states (2), (3) and (4) are shown in Fig. 12a (using the same colors as in Fig. 11).

The shapes of the G -distribution curves of the simplified finite square plate and the simplified semi-infinite circular plate of the same configuration are very similar, with the G -distribution from the latter model being more uniform and the states appearing at lower opening displacement levels, which is logical considering the much higher laminate stiffness. Thus, the fracture behavior is consistent in both models.

In both cases, the cracks initiated and propagated firstly in the $90^\circ/270^\circ$ direction, since in this direction the distance between the pre-crack front and the loading zone edge was the shortest. As the loading continued, the crack progressively initiated and propagated in each direction and finally reached full fiber bridging in all directions. Due to the large variation of the distance between the pre-crack front and the loading zone edge, the G -distribution along the pre-crack perimeter showed notable non-uniformity. For instance, when full fiber bridging appeared in the $90^\circ/270^\circ$ direction in model E3/1-C35-1.0G (Fig. 11b), crack initiation in the $0^\circ/180^\circ$ direction, within a range of around $\pm 15^\circ$, did not yet occur (see the green dashed curve in Fig. 11b and the green region in Fig. 12a). Comparing Fig. 11b to Fig. 11a, it was found that as the shortest distance between the pre-crack front and the loading zone edge became shorter, crack initiation in one direction and full fiber bridging in one direction appeared at a lower opening displacement; as the longest distance between the pre-crack front and the loading zone edge became longer, crack initiation in all directions and full fiber bridging in all directions appeared at a larger opening displacement; the G -distribution along the pre-crack front became

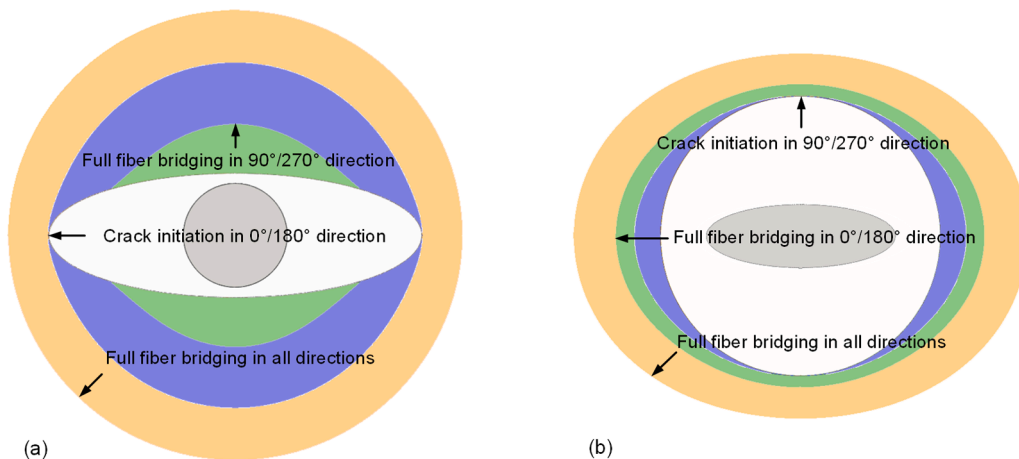


Fig. 12. Crack shapes at different fracture states: (a) E3/1-C35-1.0G; (b) C90-E3/1-1.0G.

generally less uniform.

In order to describe the overall shape evolution of the delamination in a simpler way, the crack length ratio (CLR), defined as the ratio of the crack length in the elliptical major-axis direction to that in the minor-axis direction (i.e. a_x/a_y in Fig. 8), is shown in Fig. 13 during the first 45 mm of loading. The CLR of model C90-C35-1.0G equaled a constant value of 1.0 due to its circular symmetry, denoting a circular delamination shape throughout the loading process, as was also observed in the CFM experiments. The CLR of the plates with elliptical pre-crack dropped rapidly from the original values (i.e. the aspect ratio of the elliptical pre-crack) to approximately 1.0 as full fiber bridging developed in all directions, i.e. the delamination shape changed from the original ellipse to a circle (the shape of the loading zone), as also shown Fig. 12a. This observation confirms that the pre-crack shape has only a minor effect on the final crack shape after a certain extent of crack propagation. Note that in the early stages, especially before crack initiation occurred in all directions, the delamination shape of the plates was irregular instead of elliptical due to different delays in crack initiation in different directions, see Fig. 12a.

4.2. Effect of pre-crack area

The load-opening displacement and stiffness-opening displacement curves during crack initiation and propagation for the basic and doubled pre-crack areas are shown in Fig. 14 (results from simplified semi-infinite circular plate models C90-C35-1.0G, 2C90-C35-1.0G, 2E'2/1-C35-1.0G and 2E'3/1-C35-1.0G). Since the difference between the pre-crack dimensions in the group of the same pre-crack circumference and the group of the same basic pre-crack area was small, models E'2/1-C35-1.0G and E'3/1-C35-1.0G behaved similarly to E2/1-C35-1.0G and E3/1-C35-1.0G in all respects. Hence, their results are not presented and can be referred to in the previous section (Fig. 10). The results in the group of doubled pre-crack area followed similar rules as in the group of the same pre-crack circumference, except that convergence of the curves occurred later due to the increased distances between the pre-crack front and the loading zone edge. Compared with model C90-C35-1.0G, the larger pre-crack area in 2C90-C35-1.0G resulted in smaller new crack surfaces created at the same opening displacement, and consequently led to less energy being consumed, as reflected in its slightly lower load level throughout the loading process. All models with doubled pre-crack area still had the same constant stiffness as the basic reference model (C90-C35-1.0G), confirming that the constant stiffness is independent of the pre-crack area. It is worth mentioning that, unlike the other models, 2C90-C35-1.0G did not experience softening in the beginning. On the contrary, it almost maintained the initial stiffness until crack initiation due to its special pre-crack/loading zone configuration. Indeed, the latter was not only circularly symmetric but also exhibited a distance between the pre-crack front and the loading zone edge large enough to allow a certain amount of deformation before crack initiation. After crack initiation, fiber bridging was activated and the plate entered a short stiffening stage. Then, the softening mechanism, i.e. crack propagation, prevailed over the stiffening mechanisms, i.e. fiber bridging and stretching, until full fiber bridging developed in all directions (the minimum point on the stiffness curve).

The CLR-opening displacement curves from the group of the same basic pre-crack area and the group of the same doubled pre-crack area are shown in Fig. 15. As previously discussed, the increase in the distances between the pre-crack front and the loading zone edge resulted in a delay in the occurrence of the defined fracture states. Therefore, the CLR curves for the doubled pre-crack area were smoother and reached a constant value at larger displacements. The constant CLR values for elliptical pre-cracks are very close to 1.0, i.e. the aspect ratio of the loading zone (a circle), but a slight deviation was observed, which increased as the pre-crack area and pre-crack aspect ratio increased, indicating a greater difference in the energy consumed in different directions. Essentially, different energy consumption histories in different directions finally led to slightly noncircular crack shapes at the constant-stiffness state.

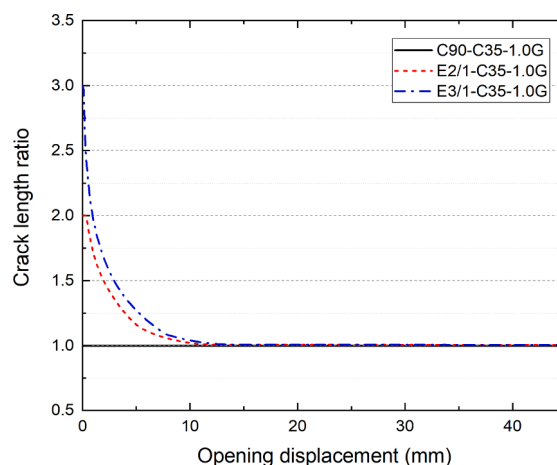


Fig. 13. Crack length ratio vs opening displacement curves for different pre-crack shapes.

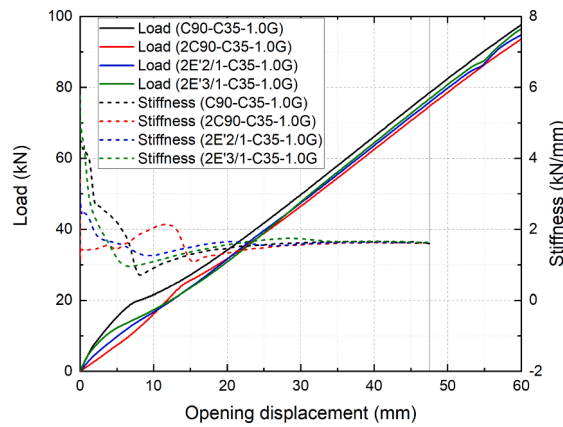


Fig. 14. Load and stiffness vs opening displacement curves during crack initiation and propagation for different pre-crack areas (simplified semi-infinite circular plate results).

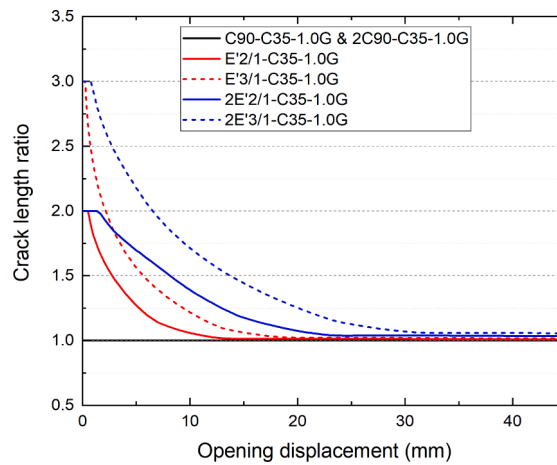


Fig. 15. Crack length ratio vs opening displacement curves for different pre-crack areas.

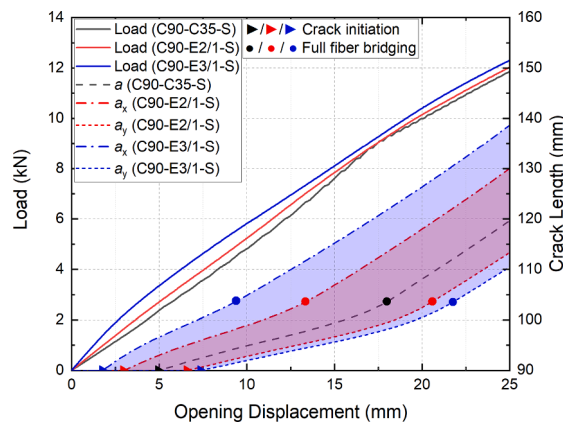


Fig. 16. Load and crack length vs opening displacement curves during crack initiation and early propagation for different loading zone shapes (simplified finite square plate results).

4.3. Effect of loading zone shape

The load-opening displacement and the crack length-opening displacement curves during crack initiation and early propagation for different loading zone shapes are presented in Fig. 16 (results from simplified finite square plate models C90-C35-S, C90-E2/1-S and C90-E3/1-S). As the aspect ratio of the loading zone increased from 1 to 3 (i.e. from a circle to a flat ellipse), the initial stiffness of the system also increased although not significantly. The shortest distance between the pre-crack front and the loading zone edge decreased from 55 mm for model C90-C35-S to around 29.4 mm for model C90-E3/1-S, which is considered the main factor causing the differences in initial stiffness. Full fiber bridging in all directions developed in all three plates, after which the three load-opening displacement curves converged and became parallel. Although different crack shapes were formed at the end of the loading, as reflected in the crack length curves, the stiffness and load levels of the three plates were very similar. This is attributed to the equal areas of the loading zones of the plates, which can be regarded as the dominant factor controlling the structural response for the cases investigated. The initial bridging lengths in the orthogonal directions, calculated from the crack length-opening displacement curves, were found to be approximately equal (~ 13.6 mm) not only within each plate but also among all three plates.

The load-opening displacement and stiffness-opening displacement curves during crack initiation and propagation for the different loading zone shapes were plotted in Fig. 17 (results from simplified semi-infinite circular plate models C90-C35-1.0G, C90-E2/1-1.0G, C90-E3/1-1.0G and C90-E4/1-1.0G). All four load-opening displacement curves converged after full fiber bridging in all directions with the same stiffness and a similar load level, in spite of different loading zones. All four plates experienced an initial rapid softening, followed by mild stiffening, and finally reached the constant-stiffness state, indicating the balance between the stiffening and softening mechanisms. The minimum points on the stiffness curves, appearing at a similar displacement level (~ 9.0 mm), corresponded to the onset of full fiber bridging in all directions, after which the curves overlapped, showing identical behavior. This shows that the loading zone shape also has a minor effect on the final constant stiffness of the system, provided that the areas of the loading zones are the same.

The normalized G-distribution along the pre-crack perimeter at the four specified fracture states, along with their corresponding displacement levels, are presented in Fig. 18 for both simplified finite square plates and simplified semi-infinite circular plate models with elliptical loading zone (C90-E2/1-S, C90-E3/1-S, C90-E2/1-1.0G and C90-E3/1-1.0G). The crack shapes in model C90-E3/1-1.0G at the last three fracture states are further illustrated in Fig. 12b. The shapes of the curves of the two models with the same configuration are similar, with the G-distribution of the simplified semi-infinite circular plate being more uniform and the states appearing at lower opening displacement levels due to the increased moduli.

Crack initiation in all directions occurred earlier in these plates than full fiber bridging in all directions. The crack also initiated and propagated firstly from the direction with the shortest distance between the pre-crack front and the loading zone edge, and the relationship between the opening displacement levels of the fracture states and the shortest/longest distance followed the same rule as discussed in the previous section, whereas in these plates, the G-distribution along the pre-crack perimeter was much more uniform. For instance, when full fiber bridging occurred in the $0^\circ/180^\circ$ direction in model C90-E3/1-1.0G, the crack had also propagated to a small extent in the $90^\circ/270^\circ$ direction (see the green dashed curve in Fig. 18b and the green region in Fig. 12b); and the crack shapes at early stages in Fig. 12b are more rounded instead of irregular as in Fig. 12a, indicating less delay in crack initiation and early propagation in different directions. Within each group of models (simplified finite square plates or simplified semi-infinite circular plates), the displacement levels of each state are fairly close between the two loading zone configurations, implying that the equivalence of the loading zone by area cannot only lead to an identical stiffness response after full fiber bridging developed in all directions, but also result in a similar fracture response in the early stages, which was also reflected in the equal bridging lengths in the simplified finite square plates (Fig. 16).

The CLR-opening displacement curves for plates with different loading zone shapes of the same basic area (results from simplified semi-infinite circular plate models C90-E2/1-1.0G, C90-E3/1-1.0G and C90-E4/1-1.0G) are presented in Fig. 19 (red curves). The CLR

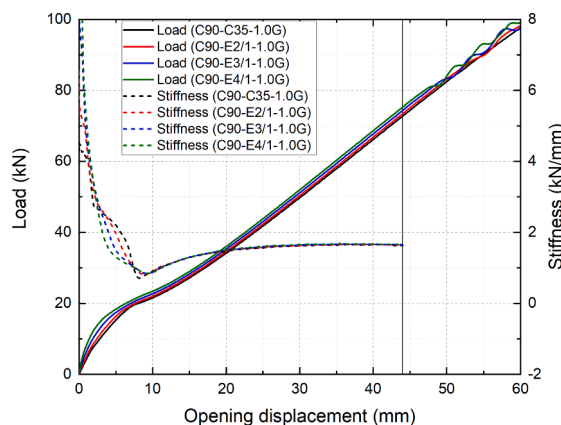


Fig. 17. Load and stiffness vs opening displacement curves during crack initiation and propagation for different loading zone shapes (simplified semi-infinite circular plate results).

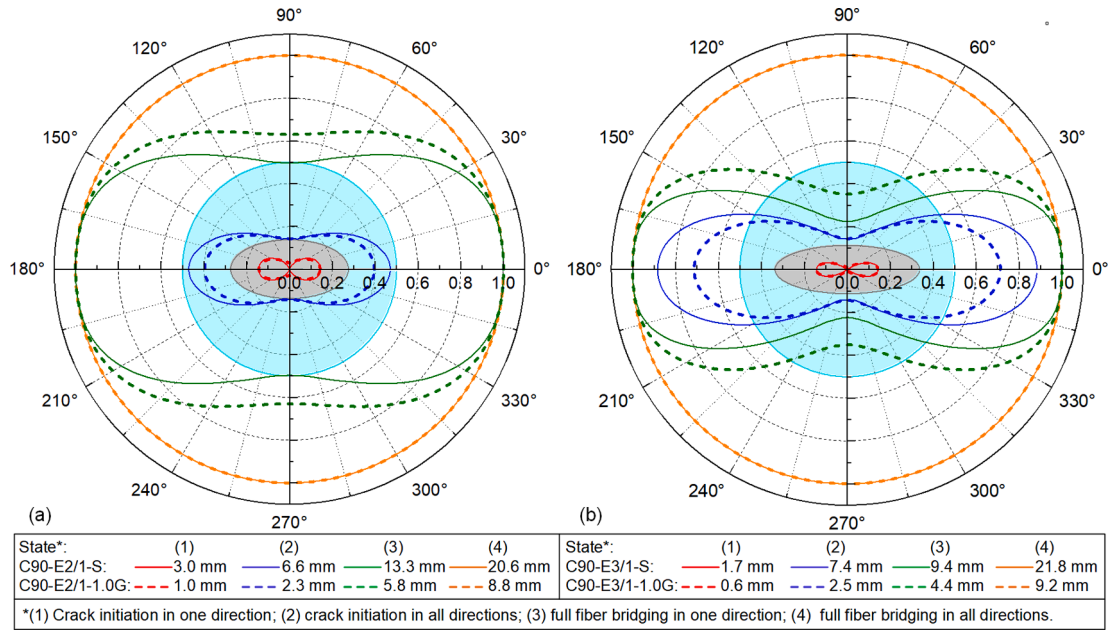


Fig. 18. Normalized G-distribution curves along pre-crack perimeter in plates with elliptical loading zone at different fracture states: (a) model C90-E2/1-S and C90-E2/1-1.0G; (b) model C90-E3/1-S and C90-E3/1-1.0G.

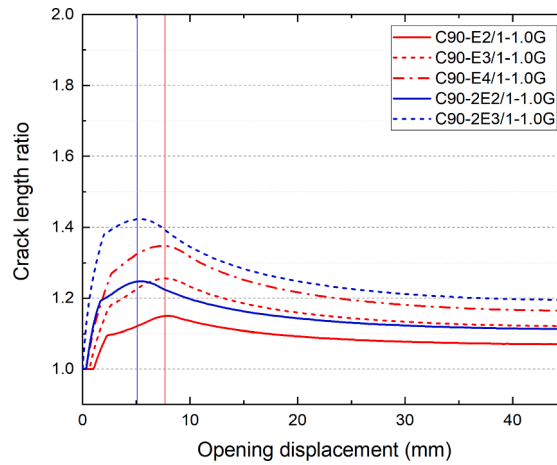


Fig. 19. Crack length ratio vs opening displacement curves for different loading zone shapes and areas.

rose sharply from 1.0 (denoting the original circular pre-crack), then slowed after the crack propagated in all directions, and reached a peak before full fiber bridging in all directions. The curves then declined slowly until they entered a plateau with a constant value above 1.0, which corresponded to the constant-stiffness state introduced above, indicating that the balance between the stiffening mechanisms and the softening mechanism was achieved in each direction after different energy consumption histories, so that the circumferential curvature of the half-laminate finally remained constant. The peaks of the CLR curves do not correspond to any specified fracture states. However, all three curves reached the peak at around the same opening displacement, indicated by a vertical red line. A higher aspect ratio of the loading zone, i.e. a flatter elliptical loading zone, resulted in a higher CLR, i.e. a flatter elliptical crack, throughout the loading, but the crack shape was generally much closer to a circle than the original shape of the loading zone. The CLR evolution corresponded to the delamination shape variation as follows: the crack propagated rapidly from the circular pre-crack in the α_x direction, until initiation occurred along the whole pre-crack front. Subsequently, the growth rates in different directions became more and more balanced and the elliptical crack more and more rounded during propagation. Eventually the constant-stiffness state was reached, where the delamination grew in an elliptical shape with constant aspect ratio.

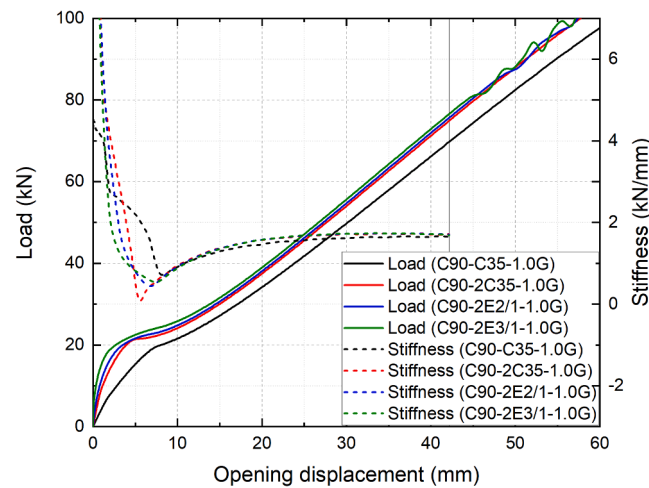


Fig. 20. Load and stiffness vs opening displacement curves during crack initiation and propagation for different loading zone areas (simplified semi-infinite circular plate results).

4.4. Effect of loading zone area

The load-opening displacement and stiffness-opening displacement curves during crack initiation and propagation for the basic and doubled loading zone areas are shown in Fig. 20 (results from simplified semi-infinite circular plate models C90-C35-1.0G, C90-2C35-1.0G, C90-2E2/1-1.0G and C90-2E3/1-1.0G). The results in the group of the same doubled loading zone area are quite similar to those from the group of the same basic area (Fig. 17), and thus will not be discussed again here. By comparing the results from models C90-C35-1.0G and C90-2C35-1.0G, it can be concluded that doubling the loading zone area increased the load levels throughout the loading process. Regarding the stiffness response, a larger loading zone area also increased the initial stiffness considerably due to shorter distances between the pre-crack front and the loading zone edge, and caused full fiber bridging in all directions to occur at a lower opening displacement level (the minimum point on the stiffness curve). Following full fiber bridging in all directions, the stiffening mechanisms of the systems prevailed over the softening mechanism for both plates until a final balance was reached, which marked the constant-stiffness state. The constant stiffness also increased slightly as the loading zone area doubled.

The CLR-opening displacement curves of models C90-2E2/1-1.0G and C90-2E3/1-1.0G are presented in Fig. 19 (blue curves). Comparing them with the red curves revealed that the general trends of the curves are very similar. However, the CLR increased as the loading zone area doubled throughout the loading process. The increase of the CLRs at the constant-stiffness state indicated that, as the loading zone area doubled, the final crack shape became slightly closer to the loading zone shape, i.e. flatter and less rounded. Doubling the loading zone area also caused the peaks to appear at a lower opening displacement level, which proved that the opening displacement level of the peak was independent of the loading zone shape (i.e. the aspect ratio) but dependent on the loading zone

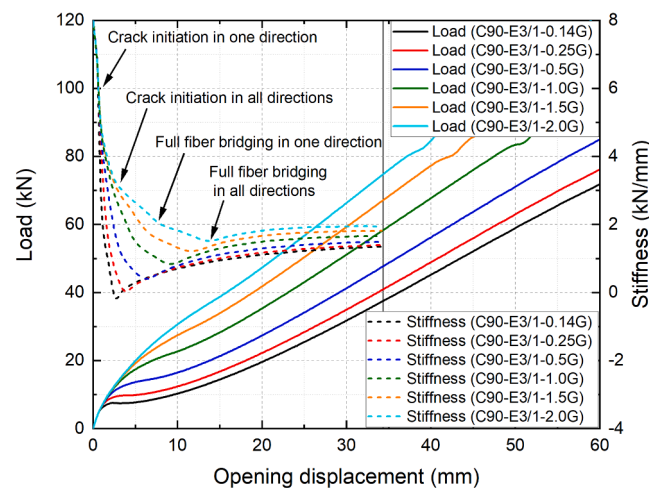


Fig. 21. Load and stiffness vs opening displacement curves during crack initiation and propagation for different fracture resistances (simplified semi-infinite circular plate results).

area.

4.5. Effect of fracture resistance

The load-opening displacement and stiffness-opening displacement curves during crack initiation and propagation for the plates with the same pre-crack/loading zone configuration but different fracture resistances are shown in Fig. 21. As the fracture resistance was increased to twice the basic value (5.6 kJ/m^2 for model C90-E3/1-2.0G), the buckling of the plate occurred at a low opening displacement level of around 34 mm, indicated by a vertical black line in the figure, and all stiffness evolutions after this level were not presented. Since the initiation components of the cohesive laws were identical, all models had the same initial stiffness and load response. As soon as the crack started to propagate, both the load and the stiffness curves deviated significantly. Higher fracture resistance resulted in higher stiffness and higher load levels throughout the loading process. In addition, increasing the fracture resistance also caused the four specified fracture states to appear at higher opening displacement levels; if the fracture resistance was high enough, all four states could be clearly identified from the stiffness curves (see the stiffness curve of model C90-E3/1-2.0G for example).

To further investigate the effect of fracture resistance on the final state of the plates, the ascending segments of the stiffness curves (the part after full fiber bridging developed in all directions) in Fig. 21 were fitted with exponential functions to extract the constant stiffness values at infinite opening displacement for this specific pre-crack/loading zone configuration. These values were then plotted against the corresponding G_{tot} value of the plate in Fig. 22. A linear relationship between the constant stiffness and G_{tot} was observed, confirming the conclusions in [28].

The CLR-opening displacement curves were plotted in Fig. 23 for plates of two circular pre-crack/elliptical loading zone configurations with three different fracture resistances. As the fracture resistance increased, the CLR at the constant-stiffness state also increased slightly (i.e. the final delamination shape turned to a flatter ellipse), and the appearance of the peaks (marked with vertical lines) of the curves were delayed to a higher opening displacement level.

The CLR at constant-stiffness state was extracted by exponential fitting of the descending segments of the CLR-opening displacement curves for plates with elliptical loading zone. The CLRs at constant-stiffness state of the plates with the C90-E3/1- configuration were then plotted against the corresponding G_{tot} in Fig. 22 to show the relationship between the final crack shape and fracture resistance. The CLR at constant-stiffness state was found to increase nonlinearly with G_{tot} , signifying that improvement of the fracture resistance made the final crack shape more similar to the loading zone shape (less rounded), but the effect became weaker as the resistance further improved.

4.6. Comparison of effects

By comparing the results in Section 4.1 and 4.3, it could be concluded that the pre-crack shape had a much stronger effect on the structural stiffness at the initiation and early propagation stages than the loading zone shape. The variation of the distances between the pre-crack front and the loading zone edge (similar to the effect of the pre-crack length in DCBs) is considered the main factor causing such differences in initial stiffness and also the G -distribution along the pre-crack perimeter. The G -distribution along the pre-crack perimeter was found to be more uniform in the plates with elliptical loading zone than those with elliptical pre-crack. Consequently, the bridging lengths in different directions at the onset of full fiber bridging in all directions are approximately the same in the former plates, but clearly differed in the latter plates.

As soon as full fiber bridging developed in all directions, the influence of both the pre-crack shape and area and the loading zone shape on the stiffness became minor. Doubling the loading zone area increased the constant stiffness, but the effect was weak. For the cases investigated, the most relevant parameter affecting the constant stiffness is the fracture resistance, and a linear relationship between them was observed. Regarding load levels, both the pre-crack area and the loading zone area had a slight influence, with the

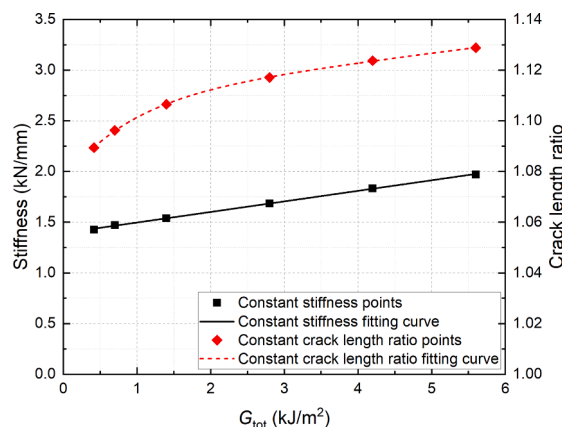


Fig. 22. Constant stiffness and crack length ratio at constant-stiffness state vs G_{tot} for C90-E3/1- configuration.

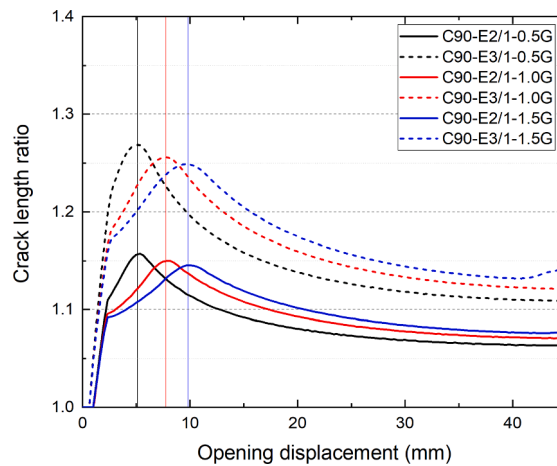


Fig. 23. Crack length ratio vs opening displacement curves for different loading zone shapes and fracture resistances.

former contributing mainly through the amount of energy consumed during crack propagation, i.e. a larger pre-crack area led to smaller new crack surfaces created at the same opening displacement level.

To investigate the effect of the loading zone shape/area and the fracture resistance on the final crack shape, the CLR at the constant-stiffness state was plotted against the loading zone aspect ratio for the plates with specific loading zone and fracture resistance combinations, as shown in Fig. 24. The sample points were augmented by simply inverting the CLR at the constant-stiffness state and the aspect ratio, meaning a 90° rotation in the calculation direction (from a_x/a_y to a_y/a_x , see Fig. 8) for each model. Subsequently, the points were sorted into three groups according to the models' loading zone area and G_{tot} , and fitted with a power function respectively, revealing a nonlinear relationship. The results show that although a higher loading zone aspect ratio (i.e. a flatter elliptical loading zone) will lead to a higher CLR (a flatter elliptical crack shape), the influence of the loading zone shape is somewhat limited. An aspect ratio of e.g. 4 only led to a CLR at the constant-stiffness state of 1.16 for model C90-E4/1-1.0G. From the fitting curves it can be concluded that the CLR at the constant-stiffness state is less sensitive to G_{tot} , as doubling the G_{tot} value only caused a slight change (also corroborated in Fig. 22 for the C90-E3/1- configuration), whereas doubling the area caused a more obvious deviation of the curves.

5. Conclusions

A numerical investigation of the 2D delamination growth in glass fiber-reinforced polymer laminates using cohesive zone modeling was carried out. The influences of the pre-crack shape/area, the loading zone shape/area and the fracture resistance on the 2D fracture behavior at crack initiation and early propagation stages and after a certain extent of crack propagation were parametrically studied, based on three types of models, i.e. a detailed finite square plate model, a simplified finite square plate model and a simplified semi-

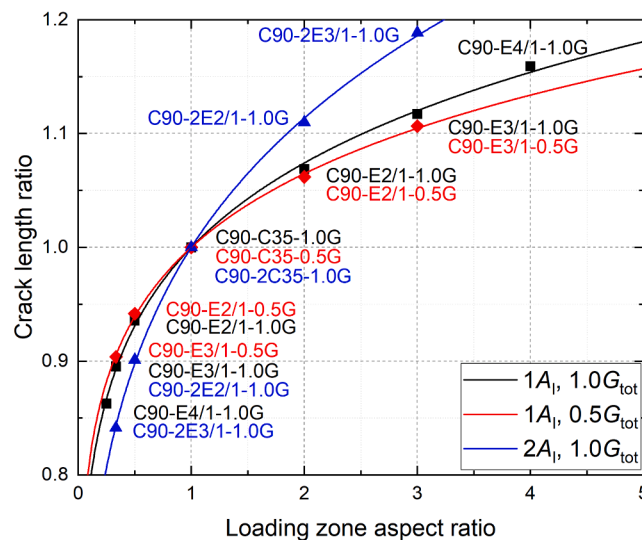


Fig. 24. Crack length ratio at constant-stiffness state vs loading zone aspect ratio for different loading zone areas and fracture resistances.

infinite circular plate model. The following conclusions could be drawn:

- Generally speaking, the plates investigated underwent an initial rapid softening stage and a slow stiffening stage under opening loads. Finally, the plates entered a state where the stiffness and crack shape became constant.
- The pre-crack shape had a strong effect on the structural stiffness and the strain energy release rate distribution along the pre-crack perimeter during crack initiation and early propagation, i.e. a flatter elliptical pre-crack resulted in a higher initial stiffness and a less uniform distribution. Therefore, the pre-crack shape in laminates plays an important role in designs where no crack propagation or only limited crack propagation is allowed, since small variations in the pre-crack shape can result in large differences in the initial stiffness and initiation load (displacement).
- A larger pre-crack area reduced the initial stiffness and load level throughout the loading process. It also delayed crack initiation and propagation.
- The loading zone shape mainly affected the crack shape during propagation, and had a moderate effect on the initial stiffness of the structure. Thus, the loading zone shape should be specifically designed according to the actual opening effects on the delamination instead of selected arbitrarily during analyses and simulations.
- After full fiber bridging in all directions, the structural stiffness became independent of the pre-crack shape/area and loading zone shape.
- Increasing the loading zone area led to slightly higher constant stiffness after full fiber bridging developed in all directions and resulted in a final crack shape more closely resembling the shape of the loading zone.
- The constant structural stiffness after full fiber bridging developed in all directions increased linearly with the fracture resistance. Higher fracture resistance also caused the final crack shape to more closely resemble the shape of the loading zone.

In the present work, a uniform cohesive law was used for the laminates in all directions throughout the loading process despite the different pre-crack/loading zone configurations. In fact, G_{br} should vary slightly among different directions and at different loading states (around $\pm 20\%$ according to initial estimations) due to the changing arm curvatures, which affect the pull-out behavior of single fibers/fiber bundles at the crack surfaces and consequently lead to slightly different fiber bridging behaviors. However, the disregard of the variation in G_{br} was considered acceptable and did not significantly affect the validity of the conclusions, since the stiffness and crack shape were not very sensitive to the change in the fracture resistance. The methodology of the present work is also applicable for orthotropic materials as long as appropriate cohesive laws in the different material directions are available.

Declaration of Competing Interest

The authors declare that they have no known competing financial interests or personal relationships that could have appeared to influence the work reported in this paper.

Acknowledgements

The authors wish to acknowledge the support and funding of this research by the Swiss National Science Foundation (Grant No. 200020_185005).

References

- [1] Bolotin VV. Delaminations in composite structures: Its origin, buckling, growth and stability. *Compos Part B Eng* 1996;27:129–45. [https://doi.org/10.1016/1359-8368\(95\)00035-6](https://doi.org/10.1016/1359-8368(95)00035-6).
- [2] Wisnom MR. The role of delamination in failure of fibre-reinforced composites. *Philos Trans R Soc A Math Phys Eng Sci* 2012;370:1850–70. <https://doi.org/10.1098/rsta.2011.0441>.
- [3] Rhead AT, Butler R. Compressive static strength model for impact damaged laminates. *Compos Sci Technol* 2009;69:2301–7. <https://doi.org/10.1016/j.compscitech.2009.01.010>.
- [4] Naya F, Pappas G, Botsis J. Micromechanical study on the origin of fiber bridging under interlaminar and intralaminar mode I failure. *Compos Struct* 2019;210: 877–91. <https://doi.org/10.1016/j.compstruct.2018.11.064>.
- [5] Canal LP, Pappas G, Botsis J. Large scale fiber bridging in mode I intralaminar fracture. An embedded cell approach. *Compos Sci Technol* 2016;126:52–9. <https://doi.org/10.1016/j.compscitech.2016.01.025>.
- [6] Sorensen L, Botsis J, Gmür T, Humbert L. Bridging tractions in mode I delamination: Measurements and simulations. *Compos Sci Technol* 2008;68:2350–8. <https://doi.org/10.1016/j.compscitech.2007.08.024>.
- [7] Shahverdi M, Vassilopoulos AP, Keller T. Modeling effects of asymmetry and fiber bridging on Mode I fracture behavior of bonded pultruded composite joints. *Eng Fract Mech* 2013;99:335–48. <https://doi.org/10.1016/j.engfractmech.2013.02.001>.
- [8] Zhao L, Gong Y, Zhang J, Chen Y, Fei B. Simulation of delamination growth in multidirectional laminates under mode I and mixed mode I/II loadings using cohesive elements. *Compos Struct* 2014;116:509–22. <https://doi.org/10.1016/j.compstruct.2014.05.042>.
- [9] Soto A, González EV, Maimí P, Turon A, Sainz de Aja JR, de la Escalera FM. Cohesive zone length of orthotropic materials undergoing delamination. *Eng Fract Mech* 2016;159:174–88. <https://doi.org/10.1016/j.engfractmech.2016.03.033>.
- [10] Brunner AJ. Experimental aspects of Mode I and Mode II fracture toughness testing of fibre-reinforced polymer-matrix composites. *Comput Methods Appl Mech Eng* 2000;185:161–72. [https://doi.org/10.1016/S0045-7825\(99\)00257-1](https://doi.org/10.1016/S0045-7825(99)00257-1).
- [11] Shahverdi M, Vassilopoulos AP, Keller T. Mixed-mode quasi-static failure criteria for adhesively-bonded pultruded GFRP joints. *Compos Part A Appl Sci Manuf* 2014;59:45–56. <https://doi.org/10.1016/j.compositesa.2013.12.007>.
- [12] Manshadi BD, Farmand-Ashtiani E, Botsis J, Vassilopoulos AP. An iterative analytical/experimental study of bridging in delamination of the double cantilever beam specimen. *Compos Part A Appl Sci Manuf* 2014;61:43–50. <https://doi.org/10.1016/j.compositesa.2014.02.001>.
- [13] Senthil K, Arockiarajan A, Palaninathan R. Experimental determination of fracture toughness for adhesively bonded composite joints. *Eng Fract Mech* 2016;154: 24–42. <https://doi.org/10.1016/j.engfractmech.2015.11.015>.

- [14] Jiang Z, Wan S, Keller T, Fang Z, Vassilopoulos AP. Influence of curved delamination front on R-curve of DCB specimen. *Compos Struct* 2019;227:111311. <https://doi.org/10.1016/j.compstruct.2019.111311>.
- [15] Davidson BD. An analytical investigation of delamination front curvature in double cantilever beam specimens. *J Compos Mater* 1990;24:1124–37. <https://doi.org/10.1177/002199839002401101>.
- [16] Jiang Z, Wan S, Zhong Z, Li S, Shen K. Effect of curved delamination front on mode-I fracture toughness of adhesively bonded joints. *Eng Fract Mech* 2015;138:73–91. <https://doi.org/10.1016/j.engfracmech.2015.03.020>.
- [17] Manshadi BD, Vassilopoulos AP, Botsis J. A combined experimental/numerical study of the scaling effects on mode I delamination of GFRP. *Compos Sci Technol* 2013;83:32–9. <https://doi.org/10.1016/j.compscitech.2013.04.016>.
- [18] Canal LP, Alfano M, Botsis J. A multi-scale based cohesive zone model for the analysis of thickness scaling effect in fiber bridging. *Compos Sci Technol* 2017;139:90–8. <https://doi.org/10.1016/j.compscitech.2016.11.027>.
- [19] Pappas GA, Botsis J. Towards a geometry independent traction-separation and angle relation due to large scale bridging in DCB configuration. *Compos Sci Technol* 2020;197:108172. <https://doi.org/10.1016/j.compscitech.2020.108172>.
- [20] Cameselle-Molares A, Vassilopoulos AP, Keller T. Experimental investigation of two-dimensional delamination in GFRP laminates. *Eng Fract Mech* 2018;203:152–71. <https://doi.org/10.1016/j.engfracmech.2018.05.015>.
- [21] Kumar P, Reddy SR. Experimental determination of interlaminar GIC using a fully embedded centre-cracked specimen. *Eng Fract Mech* 1998;59:183–9. [https://doi.org/10.1016/S0013-7944\(97\)00096-9](https://doi.org/10.1016/S0013-7944(97)00096-9).
- [22] Cameselle-Molares A, Vassilopoulos AP, Renart J, Turon A, Keller T. Numerical simulation of two-dimensional in-plane crack propagation in FRP laminates. *Compos Struct* 2018;200:396–407. <https://doi.org/10.1016/j.compstruct.2018.05.136>.
- [23] Kwon H, Kim H. Buckling and debond growth of partial debonds in adhesively bonded composite splice joints. *Compos Struct* 2007;79:590–8. <https://doi.org/10.1016/j.compstruct.2006.02.021>.
- [24] Riccio A, Raimondo A, Di Caprio F, Scaramuzzino F. Delaminations buckling and growth phenomena in stiffened composite panels under compression. Part II: A numerical study. *J Compos Mater* 2014;48:2857–70. <https://doi.org/10.1177/0021998313502742>.
- [25] Haselbach PU, Branner K. Initiation of trailing edge failure in full-scale wind turbine blade test. *Eng Fract Mech* 2016;162:136–54. <https://doi.org/10.1016/j.engfracmech.2016.04.041>.
- [26] Rhead AT, Butler R, Hunt GW. Compressive strength of composite laminates with delamination-induced interaction of panel and sublaminates buckling modes. *Compos Struct* 2017;171:326–34. <https://doi.org/10.1016/j.compstruct.2017.03.011>.
- [27] Senthil K, Arockiarajan A, Palaninathan R. Numerical study on the onset of initiation of debond growth in adhesively bonded composite joints. *Int J Adhes Adhes* 2018;84:202–19. <https://doi.org/10.1016/j.ijadhadh.2018.03.009>.
- [28] Cameselle-Molares A, Vassilopoulos AP, Renart J, Turon A, Keller T. Numerically-based method for fracture characterization of Mode I-dominated two-dimensional delamination in FRP laminates. *Compos Struct* 2019;214:143–52. <https://doi.org/10.1016/j.compstruct.2019.02.014>.
- [29] Turon A, Dávila CG, Camanho PP, Costa J. An engineering solution for mesh size effects in the simulation of delamination using cohesive zone models. *Eng Fract Mech* 2007;74:1665–82. <https://doi.org/10.1016/j.engfracmech.2006.08.025>.
- [30] Ramberg W, Osgood WR. Description of stress-strain curves by three parameters. *Natl Advis Comm Aeronaut* 1943.
- [31] Desu RK, Nitin Krishnamurthy H, Balu A, Gupta AK, Singh SK. Mechanical properties of Austenitic Stainless Steel 304L and 316L at elevated temperatures. *J Mater Res Technol* 2016. <https://doi.org/10.1016/j.jmrt.2015.04.001>.
- [32] Frossard G, Cugnoni J, Gmür T, Botsis J. Mode I interlaminar fracture of carbon epoxy laminates: effects of ply thickness. *Compos Part A Appl Sci Manuf* 2016;91:1–8. <https://doi.org/10.1016/j.compositesa.2016.09.009>.
- [33] Turon A, Camanho PP, Costa J, Renart J. Accurate simulation of delamination growth under mixed-mode loading using cohesive elements: Definition of interlaminar strengths and elastic stiffness. *Compos Struct* 2010;92:1857–64. <https://doi.org/10.1016/j.compstruct.2010.01.012>.